Model Predictive PWM for Hybrid Active Power Filter

*Yudong Li, **Shaotong Du, ***Tianyu Zhang, **** Xingguo Tan

* School of Electrical Engineering and Automation, Henan Polytechnic University, Jiaozuo 454003, Henan Province, China, (lyd@hpu.edu.cn)
** School of Electrical Engineering and Automation, Henan Polytechnic University, Jiaozuo 454003, Henan Province, China, (gdj4321@163.com)
*** School of Mechanical and Electrical Engineering, Henan Vocational College of Industry and Information Technology, Jiaozuo 454003, Henan Province, China, (zyj@hpu.edu.cn)
**** School of Electrical Engineering and Automation, Henan Polytechnic University, Jiaozuo 454003, Henan Province, China, (tanxg@hpu.edu.cn)

Abstract

Model predictive pulse-width modulation (MP-PWM) is applied to hybrid active power filter (HAPF) in this paper. The configuration, control, carried-based PWM (CPWM) and filtering performance of HAPF are described in this paper. To realize the MP-PWM, the discrete-time model of the inverter is presented and a cost function is built. The flow chart of realizing the MP-PWM is presented. The PWM is assumed as a sampling-hold circuit with an equivalent control period to compare MP-PWM and CPWM. To compare the equivalent control period of PWM, an inverter simulation with R-L-C load is carried out. The inverter simulation results verify that the equivalent control period of MP-PWM is smaller than the CPWM, while the average switching frequency is lower than the CPWM. The simulation results of HAPF with MP-PWM and CPWM show that the filter performance of HAPF with the MP-PWM is better. An experiment study of HAPF with MP-PWM has been performed to validate the MP-PWM for HAPF.

Key words

Harmonic suppression, Hybrid active power filter, Model predictive, Pulse width modulation (PWM)

1. Introduction

With the large input of nonlinear loads, the harmonic problem of the power system is becoming increasingly serious. Hybrid active power filter (HAPF), characterized with smaller rating of active power filter (APF), is one of the effective ways for harmonic suppression, which is easier to eliminate harmonics of the high-voltage grid [1]-[3].

The typical HAPF topology contains a passive power filter (PPF) and an APF, the two of which can be connected either directly or through a coupling transformer [3]. Many types of HAPF topology have been reported already [4]-[9]. Injecting the APF's current into the PPF which contains a capacitor and a fundamental resonant LC filter through a coupling transformer can greatly reduce the rating of the APF [4]-[5], But this type HAPF needs a dc power to supply the dc capacitor of the inverter. Two H -bridges are connected in series with the grid via coupling transformers which have different voltage ratios to achieve the nine-level HAPF, which can obtain high-quality voltage waveforms and reduce the switching loss [6]. The HAPF, an inverter connected with a single-tuned LC filter in series, can realize the harmonic current suppression of the diode rectifier more economically [7]-[8], which is a good scheme for the grid whose voltage is lower than 6kV. A parallel HAPF was proposed in [9], in which two inverters have different switching frequencies.

The control methods of HAPF are attracting scholars' attention. Proportional resonant （PR） controller was applied to the HAPF to achieve frequency-selective harmonic suppression [10]. Feed forward control was applied to the HAPF to improve the system's compensation performance [11], but only single order harmonic filter performance is improved in this way. Moreover, sliding mode control [12] and fuzzy control [13]-[14] were also applied to the HAPF. A double closed-current control was proposed to reduce the fundamental current of the inverter in the injection-type HAPF [15]. Hysteresis current control in [16] was applied to a three-phase four-wire HAPF.

In recent years, the model predictive control (MPC) has been widely used in various converters [17].The cost function and the discrete-time model are the key components of the MPC. The optimizing is carried out based on the value of cost function. The MPC has been applied to current control, power control, torque and flux control, capacitor voltage balancing control, etc [18]. The current control using MPC is widely used in the rectifier [19]-[20], the active power filter [21]-[22], motor drives [23], etc. The predictive control can increase the bandwidth of the active power filter [24]. The MPC has also been tried on HAPF [25], but the HAPF with more reactors and capacitors makes the model complex. The selective harmonic

elimination PWM using MPC was mentioned in [26], but the weighting factor design is difficult to be realized in HAPF, because the reference voltage of inverter is not sinusoidal. In this paper, the topology structure reported in [7] is adopted to suppress the harmonic pollution caused by the diode rectifier loads. The model predictive pulse-width modulation (MP-PWM) which is easy to be digitally realized and only needs discrete-time model of the converter is presented [27]. The HAPF with MP-PWM is studied. The MP-PWM for HAPF can have high sampling frequency. Meanwhile, the average switching frequency is lower than the sampling frequency.

The configuration，control and carrier-based PWM (CPWM) [28] of the HAPF are described in this paper. Meanwhile, the difference of filtering performance caused by CPWM using symmetrical regular sampling and asymmetric regular sampling is analyzed. The MP-PWM which contains discrete-time model, cost function and voltage optimizing is presented in detail. The MP-PWM is compared with CPWM by simulation. To provide the validity of the MP-PWM for HAPF in this paper, experiment results obtained with the diode rectifier load are provided.

2. System Description

2.1 System Configuration

Fig.1 shows the configuration of the HAPF considered in this paper. The HAPF topology consists of a LC filter which is almost resonant at 5th harmonic frequency and a converter. The HAPF is connected at the point of common connection (PCC). In Fig.1, L_S represents the supply inductance; i_{Sx}, i_{Fx} and i_{Lx} (x=A, B, C)are the supply current , compensation current and load current respectively; e_{Sx} is the supply voltage; e_x is the phase voltage at the PCC; C and L represent the capacitor and the inductance of the LC filter, respectively; S_y stands for the power switch device of the converter (y=1, 2, 3, 4, 5, 6) ; C_{dc} is dc-side capacitor and U_{dc} is the dc-bus voltage.
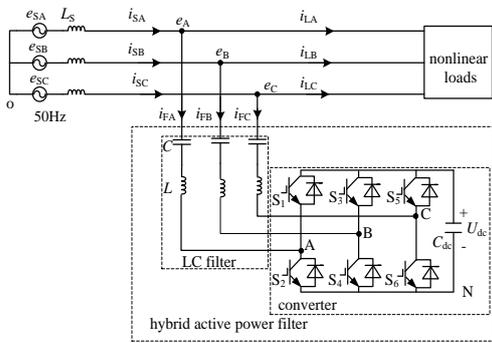

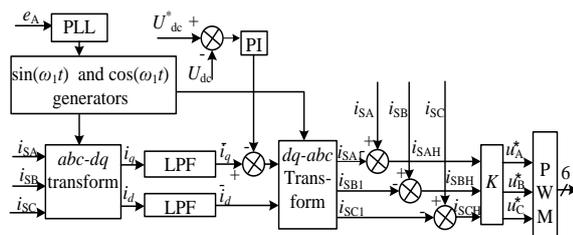Fig. 1. Configuration of the HAPF   Fig.2. Diagram of the HAPF control

2.2 System Control and Carrier-Based PWM

The control system of the HAPF is shown in Fig. 2. The harmonic detection method based on the instantaneous reactive power theory is utilized to detect the harmonic current of the supply current [7]. The *abc-dq* transformation converts the supply currents i_{SA}, i_{SB} and i_{SC} into the instantaneous active current i_d and the instantaneous reactive current i_q. The fundamental components in the supply currents correspond to dc components in i_d and i_q. Two fourth order Butterworth low-pass filters with the same cutoff frequency of 30Hz extract dc components $\bar{i}_q$ and $\bar{i}_d$ from i_d and i_q, respectively. The *dq - abc* transformation produces the supply fundamental currents i_{SA1}, i_{SB1} and i_{SC1}. Then, subtract the supply fundamental currents i_{SA1}, i_{SB1} and i_{SC1} from the supply currents i_{SA}, i_{SB} and i_{SC} to gain the supply harmonic currents i_{SAH}, i_{SBH} and i_{SCH}, respectively. Multiply the supply harmonic current i_{SxH} by the gain of K to get the reference phase voltage of the converter Ki_{SxH}. The fundamental current through the HAPF is leading, so injecting the Δi_q into the dc components $\bar{i}_q$ can regulate the dc capacitor voltage of the converter [7]. A proportional integral (PI) control is used as the control algorithm. Finally, the PWM gate signals for IGBTs can be calculated with the PWM algorithm.

The carrier-based PWM (CPWM) is widely used [28].When the digital signal processor is used to realize carrier-based PWM, symmetrical regular sampling and asymmetric regular sampling are widely used [30], which are shown in Fig. 3(a) and Fig. 3(b), respectively. T_s is the sampling period in Fig.3. In the case of symmetrical regular sampling, Fig. 3(a), sampling frequency of reference voltage is equal to the frequency. From Fig. 3(b), asymmetric regular sampling, sampling frequency is twice of the carrier frequency.
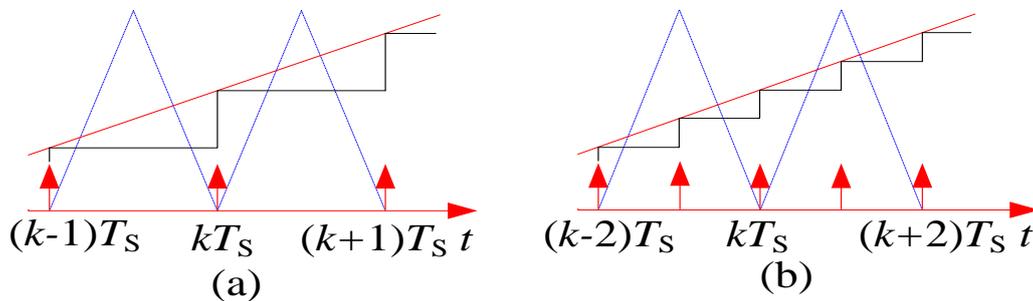

Fig.3. Sampling techniques. (a) Symmetrical regular sampling. (b) Asymmetric regular sampling

3. Filtering Characteristic Analysis

The reference voltage of the converter is Ki_{SxH} in harmonic frequencies. Neglecting the harmonics produced by on-off power device, the PWM converter can be assumed as a sampling and hold circuit with a transfer H(s)

$$H(s) = \frac{1}{T_C} \frac{1 - e^{-sT_C}}{s} \tag{1}$$

where T_C is equivalent control period and s is the Laplace operator, T_C is related to delay time.
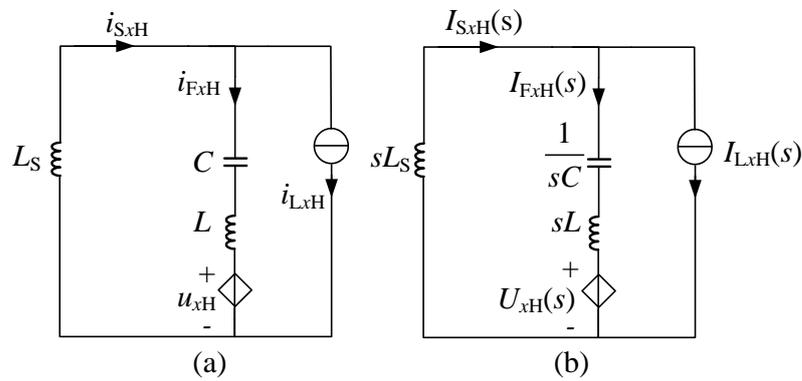

Fig. 4. Diagram of the single-phase circuit of the HAPF in the harmonic domain.(a)equivalent circuit.(b) equivalent Laplace operation circuit

Table 1. Parameters of the HAPF

L_S	0.1mH
L	4mH
C	100µF
K	30

To analyze the filtering characteristic of HAPF, a single- phase equivalent circuit of the HAPF in the harmonic domain is shown in Fig. 4(a). The u_{xH} is the inverter's output voltage. The Laplace operation circuit of the Fig. 4(a) is shown as Fig. 4(b). In Fig. 4(b), $I_{SxH}(s)$, $I_{FxH}(s)$ and $I_{LxH}(s)$ indicate the image functions of the grid harmonic current i_{SxH}, the compensation harmonic current i_{FxH} and the load harmonic current i_{LxH}, respectively; $U_{xH}(s)$ is the image function of u_{xH}.

$$U_{xH}(s) = H(s)KI_{SxH}(s) \tag{2}$$

According to Kirchholff's laws, the circuit equations from Fig. 4(b) can be obtained as

$$\begin{cases} I_{S.xH}(s) = I_{F.xH}(s) + I_{L.xH}(s) \\ sL_S I_{S.xH}(s) + \left(sL + \dfrac{1}{sC} \right) I_{F.xH}(s) + U_{xH}(s) = 0 \end{cases} \tag{3}$$

From (2) and (3), the transfer function G(s) is given as

$$\frac{I_{S.xH}(s)}{I_{L.xH}(s)} = \frac{LCs^2 + 1}{(L_S + L)Cs^2 + KCs \cdot H(s) + 1} \tag{4}$$

The characteristic of the HAPF can be observed by the bode plot of (4). The parameters shown in table 1 are adopted in this paper. From (4) and table 1, the bode plots are shown as Fig. 5.

From Fig. 5, the resonance peak is reduced when the equivalent control period T_C of PWM is smaller. In other words, harmonic amplification is reduced, the filtering performance is better. So, short equivalent control period for PWM is helpful to improve filtering performance of the HAPF.
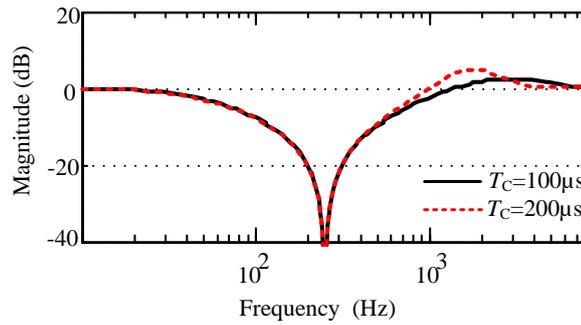

Fig. 5. Bode plots of the transfer function G(s) with TC=100µs and TC=200µs

We can know that HAPF can effectively suppress the harmonic of the supply current when K is large enough [7]. But in consideration of the stability of the HAPF control system, the value of K shouldn't be increased unlimitedly. The harmonic impedance of LC filter is small near the resonant frequency, but it increases when the frequency is far away from the resonant frequency. Therefore, when K is constant, the harmonic suppression capability of HAPF to the different frequency harmonic current of i_{Lx} varies with the changes of LC filter harmonic impedance. The characteristic is shown as in Fig. 5. In order to improve the harmonic suppression capability of HAPF, the proportion K can be updated to be the proportional resonant (PR) compensator [30]. The transfer function in the frequency domain of PR is given as follows

$$G_{PR}(s) = K_P + \sum_h^{h=5,7,\cdots} \frac{2K_{Ih}\omega_{ch}s}{s^2 + 2\omega_{ch}s + \omega_h^2} \tag{5}$$

103

where K_P is the proportional gain, K_{Ih} is the hth integral gain, ω_h is the hth harmonic angular frequency, and ω_{ch} is the hth cutoff frequency. $K_P=30$, $K_{Ih}=70$(h=7, 11, 13, 17, 19, 23, 25) and $\omega_h=1.5h$ are adopted in this paper. Replacing K with $G_{PR}(s)$, the bode plots are shown as Fig.6. From Fig.6, the filtering performance is improved. And filtering performance is also becomes better when T_C of PWM is smaller.
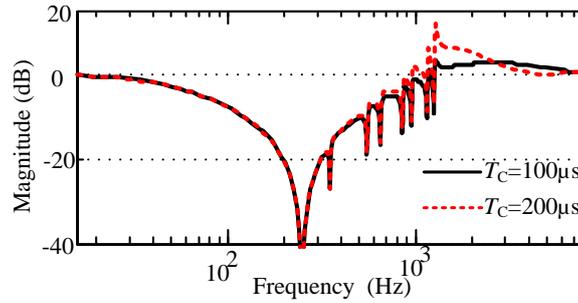

Fig. 6. Bode plots of the transfer function with T_C=100μs and T_C=200μs when PR is adopted

4. Model predictive PWM Algorithm

The sampling techniques of Carrier-based PWM are shown in Fig. 3. The difference of filtering performance between T_C=100μs and T_C=200μs is also analyzed. Simulation results in part V will show that equivalent control periods of the carried-based PWM using symmetrical regular sampling (CPWM-S) and asymmetrical regular sampling (CPWM-A) are the carrier period and twice the carrier period, respectively. To reduce control period T_C of the CPWM, the carrier frequency is increased. However, in that way the switching frequency is also increased. In this paper, the MP-PWM producing smaller equivalent control period under the same average switching frequency is applied to HAPF. The MP-PWM algorithm includes discrete converter model, cost function and selecting optimal voltage vector [27].

4.1 Discrete Converter Model

The three-phase converter is shown in Fig.1. The switching state of the power switches S_y can be represented by the switching signals s_A, s_B, and s_C defined as follows:

$$s_A = \begin{cases} 1 & \text{(if } S_1 \text{ on and } S_2 \text{ off)} \\ 0 & \text{(if } S_1 \text{ off and } S_2 \text{ on)} \end{cases} \tag{6}$$

$$s_B = \begin{cases} 1 & \text{(if } S_3 \text{ on and } S_4 \text{ off)} \\ 0 & \text{(if } S_3 \text{ off and } S_4 \text{ on)} \end{cases} \tag{7}$$

$$s_C = \begin{cases} 1 & \text{(if } S_5 \text{ on and } S_6 \text{ off)} \\ 0 & \text{(if } S_5 \text{ off and } S_6 \text{ on)} \end{cases} \tag{8}$$

From (6), (7) and (8), the converter's output voltage is

$$u_{xN} = s_x U_{dc} \tag{9}$$

where u_{xN} is the phase-to-point (N) voltage of the converter. The converter's output voltage vector can be expressed as

$$\boldsymbol{u} = \frac{2}{3}(u_{AN} + u_{BN}e^{j2\pi/3} + u_{CN}e^{j4\pi/3}) \tag{10}$$

The corresponding relations between the switching signals and the converter's output voltage vector can be calculated by (6)-(10).

Table 2. Switching Signals And Voltage Vectors

$(s_A\ s_B\ s_C)$	$000(\boldsymbol{u}_1)$	$100(\boldsymbol{u}_2)$	$110(\boldsymbol{u}_3)$
voltage vector	0	U	$Ue^{j\pi/3}$
$(s_A\ s_B\ s_C)$	$010(\boldsymbol{u}_4)$	$011(\boldsymbol{u}_5)$	$001(\boldsymbol{u}_6)$
voltage vector	$Ue^{j2\pi/3}$	$Ue^{j\pi}$	$Ue^{j4\pi/3}$
$(s_A\ s_B\ s_C)$	$101(\boldsymbol{u}_7)$	$111(\boldsymbol{u}_8)$	
voltage vector	$Ue^{j5\pi/3}$	0	

4.2 Cost Function

The reference voltages u_A^*, u_B^* and u_C^* are transformed from the *abc*-frame to the *αβ*-frame

$$\begin{bmatrix} u_\alpha^* \\ u_\beta^* \end{bmatrix} = \frac{2}{3} \begin{bmatrix} 1 & -\dfrac{1}{2} & -\dfrac{1}{2} \\ 0 & \dfrac{\sqrt{3}}{2} & -\dfrac{\sqrt{3}}{2} \end{bmatrix} \begin{bmatrix} u_A^* \\ u_B^* \\ u_C^* \end{bmatrix} \tag{11}$$

The reference voltage vector can be expressed as

$$\boldsymbol{u}^* = u_\alpha^* + ju_\beta^* \tag{12}$$

In the MP-PWM algorithm, only one voltage vector which minimizes the cost function will be chosen within a sampling interval. The established cost function is

$$g = \left| \int \boldsymbol{u}^{*} dt - \int \boldsymbol{u} dt \right| \tag{13}$$

From (13), the discrete-time equation can be obtained as

$$g(k) = \left| \sum_{m=0}^{k+1} \left[\boldsymbol{u} * (m) T_{\mathrm{s}} \right] - \sum_{m=0}^{k} \left[\boldsymbol{u}(m) T_{\mathrm{s}} \right] \right| \tag{14}$$

where T_{s} is the sampling period. In (14), the sampling interval TS is sufficiently small, it can be assumed that $\boldsymbol{u}^{*}(k+1)=u(k)$.The initial conditions in (14) are

$$\begin{cases} \boldsymbol{u} * (0) = 0 \\ \boldsymbol{u}(0) \quad = 0 \end{cases} \tag{15}$$

From (14) and (15), the converter output voltage vector $u(k)$ is only uncertain in the kth sampling interval.

4.3 Selecting Optimal Voltage Vector

The cost function (14) is as a criterion to select optimal voltage vector in the kth sampling interval from table 2. The flow diagram of selecting optimal voltage vector is shown in Fig. 7. In Fig. 7, the intermediate variables $\gamma^{\mathrm{P}}(k)$ is

$$\gamma^{\mathrm{P}}\left(k\right) = \sum_{m=0}^{k+1} \left[\boldsymbol{u} * (m) T_{\mathrm{s}} \right] - \sum_{m=0}^{k-1} \left[\boldsymbol{u}(m) T_{\mathrm{s}} \right] \tag{16}$$

Substituting (16) into (14), the $g(k)$ is

$$g(k) = \left| \gamma^{\mathrm{P}}\left(k\right) - \boldsymbol{u}\left(k\right) T_{\mathrm{s}} \right| \tag{17}$$

The execution flow is as follows:

Step 1: Interrupt response, calculate variables $\gamma^{\mathrm{P}}(k)$ and assign initial values to the intermediate variables.

Step 2: With the objective to minimize the value of cost function $g(k)$, optimization is conducted to vectors in table 2 to search the optimal voltage vector at the kth sampling interval.

Step 3: If the zero voltage vector is chosen in step 2, redundant zero vectors are chosen, which is based on the number of commutations. When the converter output voltage vector $u(k\text{-}1)$ is $u_1(000)$, $u_2(100)$, $u_4(010)$ or $u_6(001)$, the $u_1(000)$ should be the optimal voltage vector in the kth sampling time interval; otherwise, the $u_8(111)$ should be the optimal voltage vector.

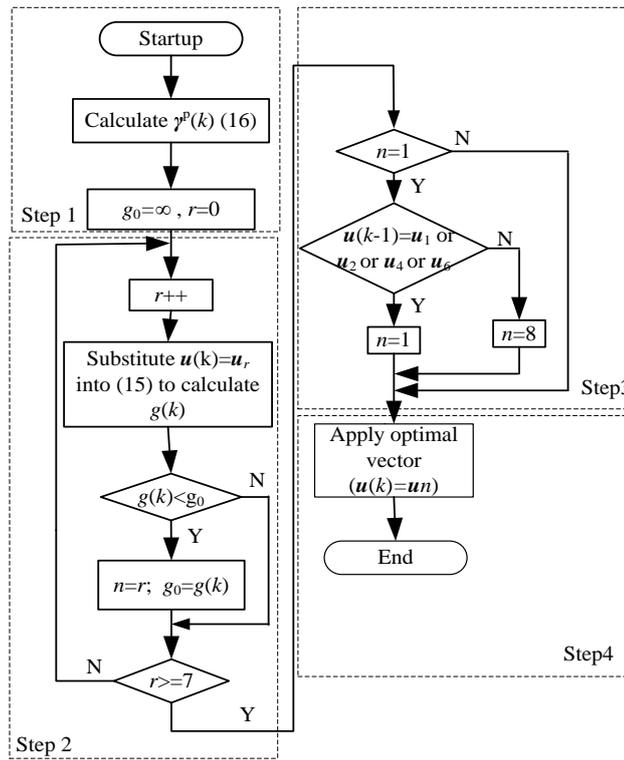Step 4: Apply optimal voltage vector, the interrupt is stopped.

Fig. 7. Flow chart of the proposed PWM

5. Simulation Results

In order to analyze the characteristics of the MP- PWM and verify its effectiveness, simulation is carried out in this paper. Switching frequency of MP-PWM is varying .To observe the switching frequency characteristics, the average switching frequency is thus defined as follow [27]

$$f = \frac{w_a + w_b + w_c}{3} \cdot \frac{1}{T} \tag{18}$$

where w_a, w_b and w_c are respectively the total number of rising edges of the signals s_A, s_B and s_C at the time of T, $T=20$ms.

5.1 Inverter Results

Matlab simulation software is adopted to simulate and analyze the results. To analyze the equivalent control period T_C of PWM, an inverter circuit simulation was set up. The inverter circuit is shown as Fig. 8. In Fig. 8, the L and C are resonant at 550Hz. The reference voltages of PWM are three- phase symmetrical sinusoidal voltages. The frequency of reference voltages is 550Hz. In the invert circuit, the load impedance is 1Ω at 550Hz, so the load current is the expression of converter's output voltage at 550Hz. The load impedance is large at other frequencies, so the load current is almost sinusoidal.

The performances of CPWM and MP-PWM have been first verified via computer simulation, respectively. The carrier frequency and sampling frequency $1/T_S$ of MP-PWM are 2.5 kHz and 10 kHz, respectively. Simulation waveforms are shown in Fig. 9. In Fig. 9(a), f_1 and f_2 are the average switching frequency of CPWM and MP-PWM, respectively. From Fig. 9(a), the average switching frequency of MP-PWM f_2 is lower.

The reference voltage wave and load current waves are shown in Fig. 9(b). From Fig. 9(b), the reference voltage phase is lead the load current phase, however, the load current phase with MP-PWM is lead the load currents phase with CPWM-A and CPWM-S.

The response curves of transfer $H(s)$ with $T_C=130\mu s$ and $T_C=200\mu s$ under inputting the A-phase reference voltage are curves q1 and q3 shown as in Fig. 9(c), respectively. The load currents of MP-PWM and CPWM-A are curves q2 and q4, respectively. The q1 and q2 are almost overlapping. So as q3 and q4. From Fig. 9(c), the MP-PWM is equivalent to the $H(s)$ with $T_C=130\mu s$ and the S-CPWM is equivalent to the $H(s)$ with $T_C=200\mu s$. Inverter simulation results prove that the MP-PWM with lower switching frequency has smaller equivalent control period T_C.
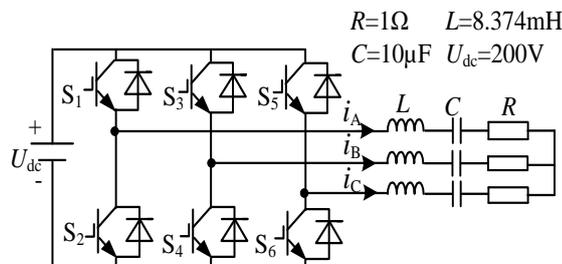

Fig. 8. The simulation inverter circuit

(a)   (b)   (c)
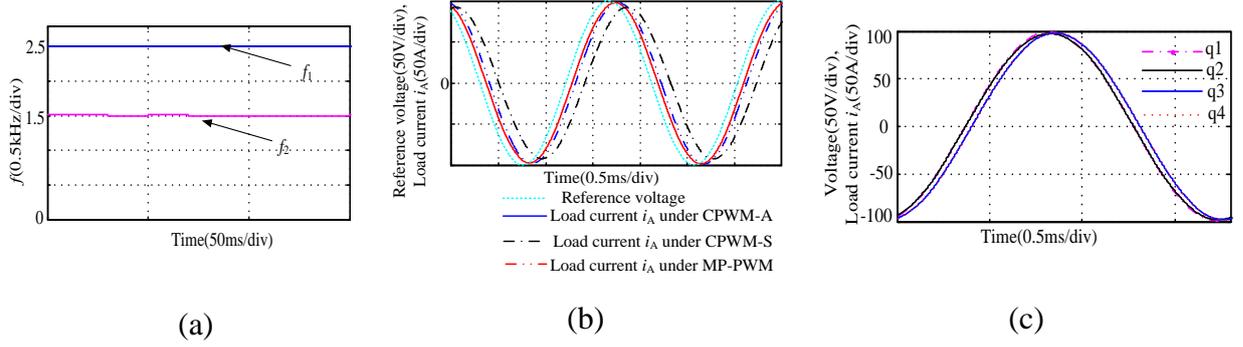
Fig. 9. The waveforms of inverter simulation (CPWM-A and CPWM-S with carrier frequency are 2.5kHz, MP-PWM with sampling frequency is 10kHz). (a) Average switching frequency. (b) Reference voltage and load currents. (c) Response curves of $H(s)$ with T_C=130μs and T_C=200μs under inputting the reference voltage and load currents of CPWM-A and MP-PWM

5.2 HAPF Results

The fully mechanized coal mining face supply voltage and the six-pulse diode rectifiers are chosen for the simulation, where the rectifier's DC-Bus is RC load. The PR compensation is adopted. The HAPF simulation with MP-PWM, CPWM-A and CPWM-S are carried out, respectively. The key parameters of the simulation are shown in table 3.

Table 3. Simulation parameters

parameters	value
Grid line voltage (RMS)	1140V
Supply inductance: L_S	0.1mH
DC capacitance of the rectifier	3000μF
Load resistance of the rectifier	10Ω
AC inductor of the rectifier	1.5mH
Filter inductor : L	4mH
Filter capacitor: C	100μF
DC voltage of the active filter: U_{dc}	600V
DC capacitance of the converter： C_{dc}	1000μF
sampling frequency of MP-PWM	10kHz
carrier frequency of CPWM-S	5kHz
carrier frequency of CPWM-A	2.5kHz

Fig. 10 shows that the simulation waveforms of the HAPF with the MP-PWM. The HAPF is switched into the grid and only regulates the dc capacitor voltage at the beginning, and then harmonic suppression begins at 0.3s in Fig. 10. Fig. 10(a) shows the waveform diagrams of the load three-phase currents i_{LA}, i_{LB} and i_{LC}. Fig. 11(a) shows the spectrum of i_{LA}. Fig. 10 (b) shows the waveform diagrams of the grid three-phase currents i_{SA}, i_{SB} and i_{SC}. Fig. 11(b) shows the spectrum of i_{SA} when the harmonic suppression is steady. Fig. 10(c) shows the waveform diagram of the dc bus voltage U_{dc}. Fig. 10(d) shows the waveform diagram of the average

switching frequency f with T=20ms. Fig. 11(c) and Fig. 11(d) show the spectrum diagrams of the grid a-phase currents when the HAPF with CPWM-S and CPWM-A is switched into the grid, respectively. The data of the special order components (1st, 5th, 7th, 11th, 13th, 17th, 19th, 23th, 25th, 29th, 31th, 35th orders) of the load a-phase current and the grid a-phase currents are listed in table 4 when the HAPF with MP-PWM, CPWM-A and CPWM-S is switched into the grid, respectively.

From Fig. 10(a) and 10(b), we can see that the grid currents become sinusoidal after the harmonic suppression is begins and that its dynamical filtering performance is good. From Fig.10(c), the dc bus voltage is regulated at 600V. From Fig. 10(d), the average switching frequency is changing but its maximum value is approximately 2.5 kHz.

Comparing Fig.11(a) with 11(b), We can see the total harmonic distortion THDs of the load current and the grid current are 27.38% and 2.73%, respectively. The filtering performance of the HAPF with MP- PWM is good. Moreover, the harmonic components (5th, 7th, 11th, 13th, 17th, 19th, 23th, 25th orders) of grid currents are all reduced shown the table 4. From Fig. 11(c), the THD of grid current is 2.90% when the CPWM-S with carrier frequency being 5 kHz. From Fig. 11(d), the THD of grid current is 3.15% when the CPWM-A with carrier frequency being 2.5 kHz. From Fig. 11 and table 4, we can see that the filtering performance of the HAPF with MP-PWM is the best.
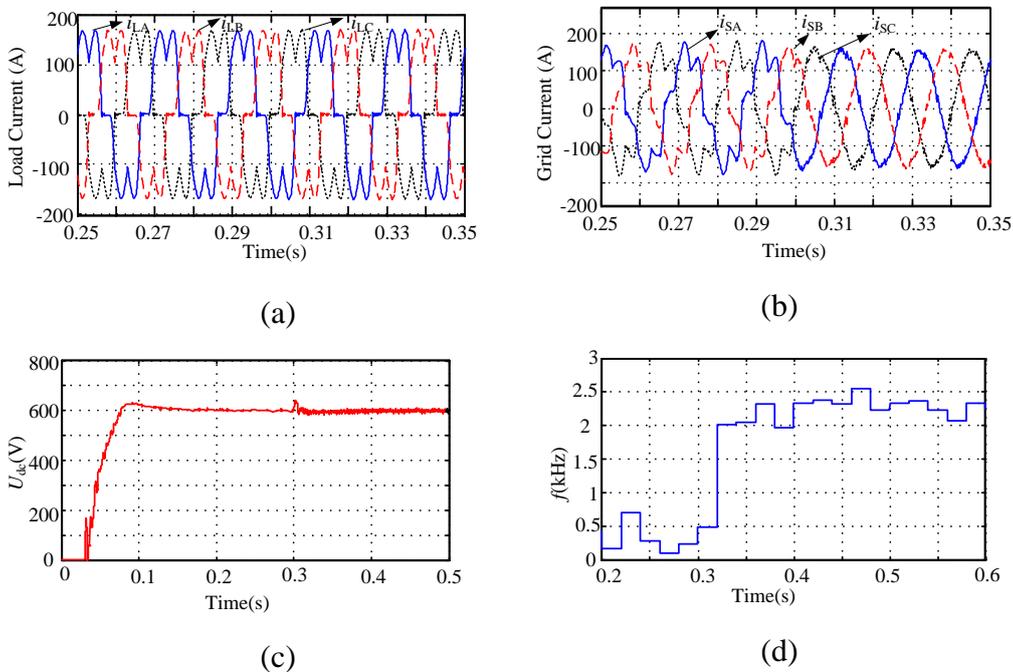

Fig. 10. The simulation waveforms of the HAPF with MP-PWM. (a) Waveforms of the load currents. (b) Waveforms of the grid currents. (c) The waveform of dc-bus voltage. (d) The average switching frequency with T=20ms
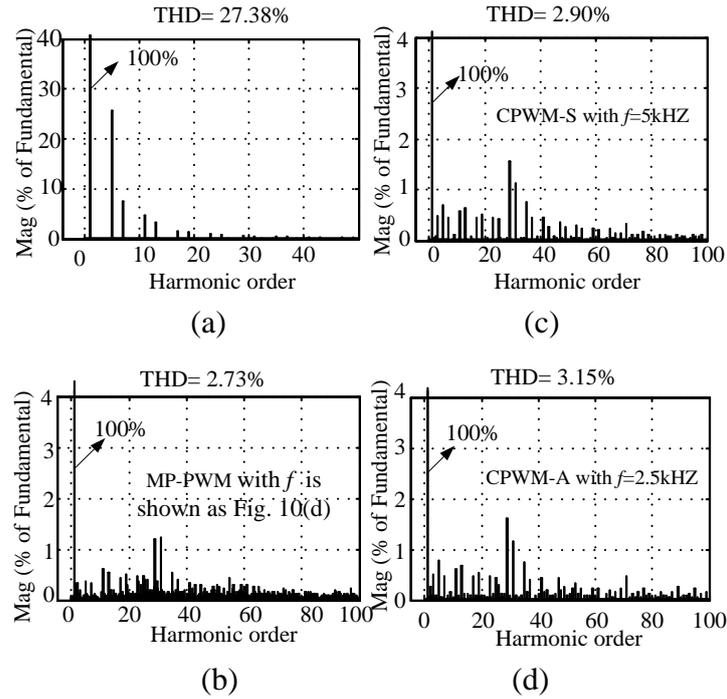
110

Fig.11. The simulation spectrum diagrams of the load a-phase current and grid a-phase currents. (a) The spectrum of load a-phase current. (b) The spectrum of a-phase grid current with MP-PWM. (c) The spectrum of a-phase grid current with CPWM-S. (d) The spectrum of a-phase grid current with CPWM- A

Table 4. Comparative Data of the load a-phase current and the grid a-phase current (peak, in amperes)

	1-order	5-order	7-order	11-order	13-order	17-order
load current	161.45	41.27	12.17	7.40	5.16	2.39
MP-PWM	155.42	0.58	0.50	0.93	0.83	0.69
CPWM-A	155.12	1.23	0.72	0.93	1.03	0.7
CPWM-S	155.65	1.08	0.7	0.89	0.99	0.69
	19-order	23-order	25-order	29-order	31-order	35-order
load current	2.20	1.50	1.18	0.95	0.84	0.63
MP-PWM	0.79	0.74	0.73	1.85	1.54	0.81
CPWM-A	0.83	0.70	0.69	2.51	1.81	1.15
CPWM-S	0.81	0.68	0.66	2.44	1.74	1.16

6. Experiment Results

In this paper, experimental verification is conducted on HAPF with MP-PWM to verify the

111

feasibility of this algorithm in laboratory. The power switch of the converter chosen for the experiment is BSM50GB120DLC. The digital signal processor TMS320F2812 is employed. The supply line voltage is 100V. The DC-bus voltage of the converter is 30V. The load is six-pulse diode rectifier which contains an AC inductance and DC resistor. AC inductance and DC resistor of rectifier are 3.1mH and 20Ω, respectively. The inductance and capacitor of the PPF are 4mH and 100μF, respectively. The FLUKE435 are also employed. The sampling frequency is 10 kHz.

(a)   (b)   (c)

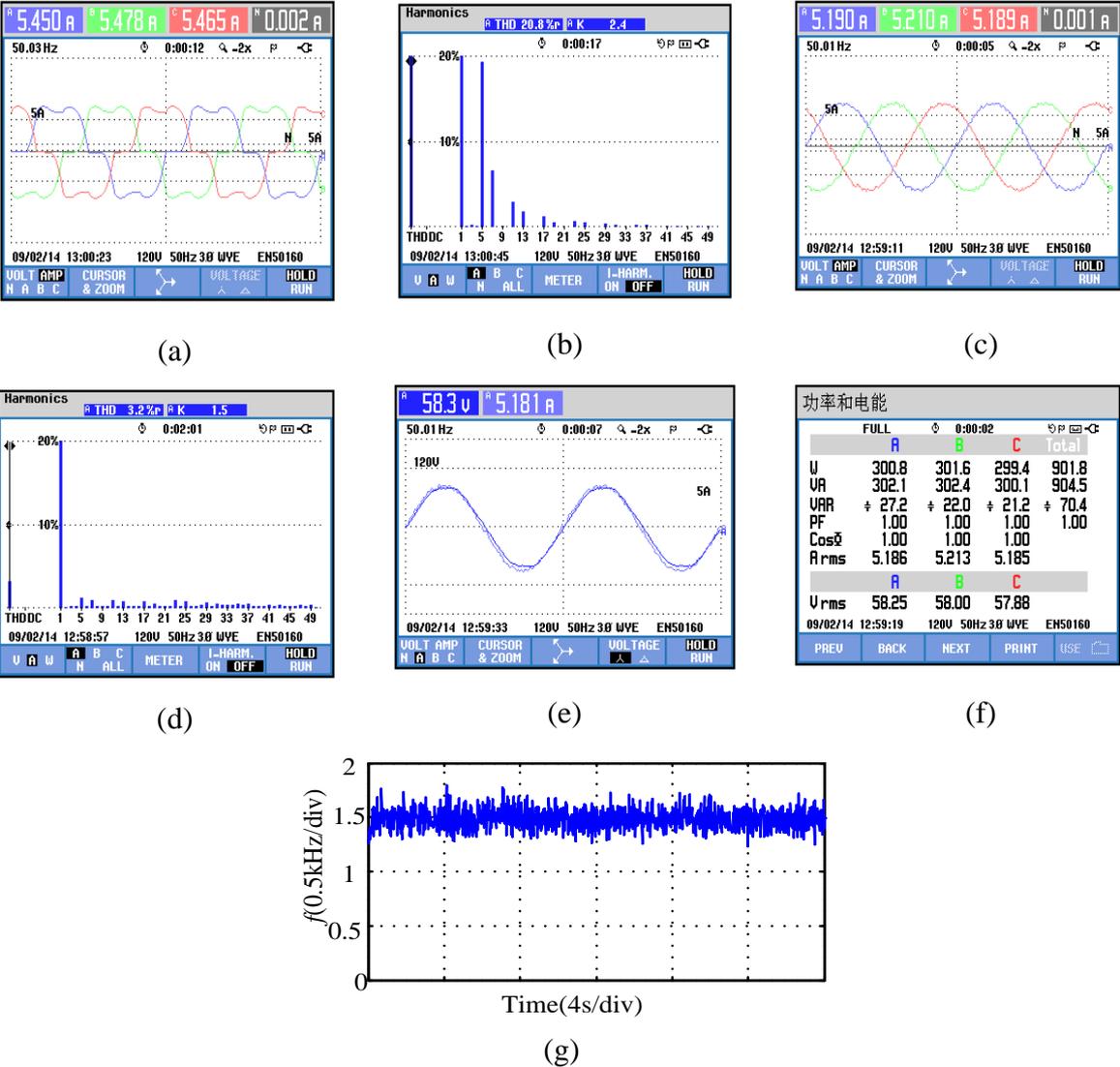(d)   (e)   (f)

(g)

Fig.12. The waveforms of HAPF with MP-PWM.
(a) The waveforms of the load currents. (b) The spectrum of load a-phase current. (c) The waveforms of the grid current when HAPF with MP-PWM is switched into the grid. (d) The spectrum of grid a-phase current when HAPF with MP-PWM is switched into the grid.(e) The waveforms of grid a-phase voltage and grid a-phase current when HAPF with MP-PWM is switched into the grid.(f) The power when HAPF with MP-PWM is switched into the grid. (g) The average switching frequency of MP-PWM

112

Fig. 12 describes the experimental waveforms. Fig. 12 (a) and 12(b) show respectively the load current and spectrum of load a-phase current, which indicates serious current distortion; Fig.12 (c) and 12(d) are respectively the grid current waveform and spectrum of grid a-phase current when HAPF with MP-PWM is switched into the grid. It can be seen from the Fig.12(c) that the current approaches to the sine. From Fig.12(b) and 12(d), the THD of a-phase current is reduced to 3.2% at the grid side from 20.8% at the load side. Fig.12 (e) is the grid a-phase voltage and the grid a-phase current. Fig.12(f) is the power and power factor. From Fig.12(e) and 12(f), the power factor is almost 1. The data of average switching frequency of MP-PWM which is calculated in DSP is plotted as Fig.12(f) using Matlab. It can be seen from Fig.12(f) that the average switching frequency is approximately 1.5 kHz and its maximum value approaches 1.8 kHz. Fig.12 indicates that HAPF with MP-PWM has effective harmonic compensation.

7. Conclusions

The system and filtering principle based on a kind of HAPF are analyzed in this paper. An MP-PWM for HAPF is presented. The inverter simulation results have demonstrated the equivalent control time of MP-PWM is smaller than CPWM-A and CPWM-S when the average switching frequency of MP-PWM is 1.5kHz, the carrier frequency of CPWM is 2.5kHz. The HAPF simulation results have demonstrated the filtering performance of the HAPF with MP-PWM is better than CPWM when the carrier frequencies of CPWM-S and CPWM-A are respectively 5kHz and 2.5kHz, the maxim average switching frequency of MP-PWM is almost 2.5kHz. The THD of load currents is 20.8% in the experiment. Results of the experiment show the THD of grid currents is reduced to 3.2%, the power factor is 1 when the HAPF with MP-PWM whose average switching frequency is approximately 1.5 kHz is switched into the grid.

References

1. P.F. Zheng, H. Akagi, and A. Nabae, A new approach to harmonic compensation in power systems-a combined system of shunt passive and series active filters, 1990, IEEE Transactions on Industry Applications, Vol. 26, No.6,pp. 983-990,

2. H. Akagi, Active harmonic filters, 2005, Proceedings of the IEEE, Vol.93, No.12, pp. 2128-2141.

3. J. H. Sung, S. Park, and K. Nam, New hybrid parallel active filter configuration minimising active filter size, 2000, IEE Proceedings - Electric Power Applications, Vol.147, No.2, pp.93-98.

4. S. Z. Kang, L. An, Z. W. Ji et. al. Study on a novel hybrid active power filter applied to a High-Voltage grid, 2007, IEEE Transactions on Industry Applications, Vol.54, No.5, pp. 2697-2704.

5. L. An, T. Ci, S. Z. Kang et. al. A Novel Three-Phase Hybrid Active Power Filter With a Series Resonance Circuit Tuned at the Fundamental Frequency, 2009 , IEEE Transactions on Industry Applications, Vol.56, No.7, pp. 2431-2440.

6. A. Varschavsky, J.Dixon, M.Rotella, and L.Morán, Cascad- -ed nine-level inverter for hybrid-series active power filter, using industrial controller，2010，IEEE Transactions on Industry Applications，Vol.57, No.8, pp.2761-2767.

7. H.Akagi, and K.Isozaki, A hybrid active filter for a three-phase 12-pulse diode rectifier used as the front end of a medium-voltage motor drive, 2012, IEEE Transactions on Power Electronics, Vol. 27,No.1, pp.69-77.

8. N.Hatti, K. Hasegawa, and H.Akagi, A 6.6-kV Transformerless Motor Drive Using a Five-Level Diode-Clamped PWM Inverter for Energy Savings of Pumps and Blowers, 2009, IEEE Transactions on Power Electronics, Vol. 24,No.3, pp:796-803.

9. A. Bhattacharya, C. Chakraborty, and S. Bhattacharya, Parallel-Connected Shunt Hybrid Active Power Filters Operating at Different Switching Frequencies for Improved Performance, 2012, IEEE Transactions on Industrial Electronics.Vol.59, No.11, pp.4007-4018.

10. L. An, P. S. Jian, W. C. Ping et. al., Power Electronic Hybrid System for Load Balancing Compensation and Frequency-Selective Harmonic Suppression, 2012, IEEE Transactions on Industrial Electronics, Vol.59, No.2, pp.723-732.

11. S. Srianthumrong, and H.Akagi, A medium-voltage transformerless AC/DC power conversion system consisting of a diode rectifier and a shunt hybrid filter, 2003, IEEE Transactions on Industry Applications. Vol.39, No.3, pp/ 983-990.

12. A. Hamadi, S. Rahmani and K. Al-Haddad, Sliding mode control of Three-Phase Shunt Hybrid Power Filter for Current Harmonics Compensation, 2010, Proceeding of IEEE_ISIE, pp. 1076-1082.

13. W. H. Choi, C. S. Lam, M. C.Wong, An Adaptive Source Current THD Oriented Fuzzy Logic Controller in Hybrid Power Filter, 2011, Proceeding of IEEE_APEC, pp. 1557-1563.

14. L. An, S. Z. Kang, Z. W. Jin et. al., Development of Hybrid Active Power Filter Based on the Adaptive Fuzzy Dividing Frequency-Control Method, 2009, IEEE Transactions on Power Delivery, Vol. 24,No.1, pp.424-432.

15. S. Z. Kang, L. An, S. John et. al., Double Closed-Loop Control Method for Injection-Type Hybrid Active Power Filter, 2011, IEEE Transactions on Power Electronics, Vol. 26,No.9, pp.2393-2403.

16. C. S. Lam, M. C. Wong, Y.D. Han, Hysteresis current control of hybrid active power filters, 2012, IET Power Electronics, Vol.5, No.7, pp. 1175-1187.

17. J. Rodriguez, M. P. Kazmierkowski, J. R.Espinoza et.al., State of the Art of Finite Control Set Model Predictive Control in Power Electronics, 2013, IEEE Transactions on Industrial Informatics, Vol.9, No.2, pp.1003-1016.

18. J. Rodriguez, C. Patricio, Predictive control of power converters and electrical drives, 2012, John Widely & Sons, pp.31-33．

19. J. Rodriguez, J. Pontt, A. C. Silva, et al., Predictive current control of a voltage source inverter, 2007, IEEE Transactions on Industrial Electronics, Vol. 54, No.1, pp.495-503.

20. R. Vargas, P. Cortes, U. Ammann et. al., Predictive Control of a Three-Phase Neutral-Point-Clamped Inverter, 2007, IEEE Transactions on Industrial Electronics, Vol.54, No.5, pp. 2697-2705.

21. J. D. Barros, J. F. Silva, Optimal Predictive Control of Three-Phase NPC Multilevel Converter for Power Quality Applications, 2008, IEEE Transactions on Industrial Electronics, Vol.55, No.10, pp.3670-3681.

22. M. Rivera, V. Yaramasu, A. Llor et. al., Digital Predictive Current Control of a Three-Phase Four-Leg Inverter, 2013, IEEE Transactions on Industrial Electronics, Vol.60, No.11, pp.490 3-4912.

23. K. B. Lee and F. Blaabjerg, Improved sensorless vector control for induction motor drives fed by a matri converter using nonlinear modeling and disturbance observer, 2006, IEEE Transactions on Energy Conversions, Vol.21, No.1, pp.52 -59.

24. F. Defaÿ A.-M. Llor, M. Fadel, A Predictive Control With Flying Capacitor Balancing of a Multicell Active Power Filter, 2008, IEEE Transactions on Industrial Electronics, Vol.55, No.9, pp.3212 -3220.

25. H. Geng, G. Yang, X. David et.al., Model Predictive Control for Transformerless Shunt Hybrid Power Filters, 2010, Proceeding of IEEE_ IPEC , pp. 2265-2270.

26. S. Kouro, B.L.Rocca. P. Cortes et.al., Predictive control based selective harmonic elimination with low switching frequency for multilevel converters, 2009, Proceeding of IEEE_ ECCE , pp. 3130-3136.

27. D. Shaotong, W. Xiaojie, Z. Juan et. al. A Novel Algorithm of PWM using virtual flux model prediction, 2015, Proceeds of the CSEE, Vol. 35, No.3, pp. 688-694.

28. J. Holtz, Pulse width Modulation for electronic power conversion, 1994, Proceeds of the IEEE, Vol. 82, No.8, pp. 1194-1214.

29. Lianjun Hu, Ling Tang, Quan Pan et. al., Research and Analysis of PI Control Strategy Based on Neural Network in Power Grid, 2016, Mathematical Modelling of Engineering Problems, Vol.3, No.1, pp.25-29.

30. R. Teodorescu, F. Blaabjerg, M. Liserre et al, Proportional- resonant controllers and filters for grid-connected voltage-source converters, 2006, IEE Proceedings-Electric Power Applications, Vol.153, No.5, pp.750-762.

31. Hua Li and Le L, Application of Fuzzy Control in PV- Storage Distributed Generation System, 2016, Review of Computer Engineering Studies, Vol. 3, No. 1, pp.11-15.